

Synthesis and characterization of antibacterial magnetite-activated carbon nanoparticles

Journal of Chemical Research
2020, Vol. 44(1-2) 80–87
© The Author(s) 2019
Article reuse guidelines:
sagepub.com/journals-permissions
DOI: 10.1177/1747519819883884
journals.sagepub.com/home/chl



Roonak Golabiazar¹, Zagros A Omar¹, Rekar N Ahmad¹,
Shano A Hasan¹ and S Mohammad Sajadi^{2,3} 

Abstract

Magnetite iron oxide nanoparticles synthesized using the co-precipitation methods were further functionalized with activated carbon. The magnetite-activated carbon nanoparticles were characterized by scanning electron microscopy equipped with energy dispersive X-ray spectroscopy, transmission electron microscopy, X-ray diffraction, Fourier transform infrared spectroscopy, and UV-Vis spectroscopy. X-ray diffraction and Fourier transform infrared confirmed the functionalization of the Fe₃O₄ nanoparticles with the activated carbon. The X-ray diffraction studies demonstrate that magnetite-activated carbon nanoparticles were indexed into the spinel cubic lattice with a lattice parameter of 0.833 nm and an average particle size of about 14 nm. Various parameters such as dislocation density, microstrain, and surface morphological studies were calculated. However, this work implicated the use of magnetite-activated carbon nanoparticles in antibacterial studies. Further, the antibacterial effect of magnetite-activated carbon nanoparticles was evaluated against three pathogenic bacteria, which showed that the nanoparticles have moderate antibacterial activity against both Gram-positive (*Staphylococcus aureus*) and Gram-negative (*Proteus mirabilis* and *Pseudomonas aureginosa*) pathogenic bacterial strains in the presence of different magnetite-activated carbon nanoparticle concentrations at room temperature.

Keywords

antibacterial activity, Gram-negative, Gram-positive, iron oxide, magnetite-activated carbon nanoparticles

Date received: 1 May 2019; accepted: 1 October 2019

Introduction

During the last decade, there has been an increasing interest in developing and understanding of matter at nanoscale,^{1,2} as they represent an intermediate dimension between bulk materials and atoms/molecules.³ Nowadays, the most well-known nanomaterials are the inorganic compounds due to their novel and improved physical, chemical, and biological properties.^{3–7} Inorganic nanomaterials exhibit very good electric, optical, electronic, magnetic, and biological properties, and are widely used in pharmaceutical, medical, and environmental applications.^{8–14} Due to the resistance of medicinal nanomaterials toward microorganisms, many researchers have turned toward engineered nanoparticles (NPs) for solving this problem. Recent advancement in the field of nanotechnology has provided attractive method for synthesizing alternative antimicrobial agents and reducing biofilm formation.¹⁵ In the area of antibacterial agents, metal NPs are of a particular interest because they can be synthesized with high surface areas and highly potential active

sites.¹⁶ A distinct class of metal oxide with distinctive magnetic properties and superior biocompatibility is found in magnetite iron oxide nanoparticles (MIONs).¹⁷ MIONs with particle sizes less than 100 nm, have been developed for a wide range of biomedical applications. Examples include contrast agents for magnetic resonance imaging (MRI),^{18–22} hyperthermia agents,²³ and carriers for targeted drug delivery to treat several types of cancer.²⁴ Specifically, the research group cultured osteoblast (bone-forming cells) with MIONs (at 4.25 mg mL⁻¹ concentration) and found that the cell density was greatly enhanced in the presence of MIONs compared with cells cultured without NPs.²⁵ The MIONs can also produce antimicrobial effects on different microorganisms such as *Staphylococcus aureus*, *Xanthomonas*, *Escherichia coli*, and *Proteus vulgaris* bacterial species.¹⁷ Lee et al.²⁶ stated that zero-valent iron NPs with size of 10–80 nm caused the inactivation of *E. coli* bacteria. Taylor and Webster²⁷ also described concentration-dependent bacteria inhibition on *Staphylococcus epidermidis* when incubated with MIONs concentrations of 100 µg mL⁻¹, 1 and 2 mg mL⁻¹.

¹Department of Chemistry, Faculty of Science, Soran University, Soran, Iraq

²Department of Nutrition, Cihan University-Erbil, Erbil, Iraq

³Scientific Research Centre, Soran University, Soran, Iraq

Corresponding author:

Roonak Golabiazar, Department of Chemistry, Faculty of Science, Soran University, PO Box 624, Soran, Kurdistan Regional Government, Iraq.
Email: rgolabiazar@yahoo.com

In this study, for the first time, we report a simple, low-cost, and environmental friendly method for preparing magnetite iron oxide-activated carbon NPs ($\text{Fe}_3\text{O}_4@\text{C}$ NPs) via a co-precipitation method. The structural properties of synthesized NPs were characterized by scanning electron microscopy (SEM) equipped with energy dispersive X-ray spectroscopy (EDS), transmission electron microscopy (TEM), X-ray diffraction (XRD), Fourier transform infrared (FTIR), and UV-Vis spectroscopy. In addition, the antibacterial activity of the $\text{Fe}_3\text{O}_4@\text{C}$ NPs was evaluated against Gram-positive (*S. aureus*) and Gram-negative (*Proteus mirabilis* and *Pseudomonas aeruginosa*) bacteria in the presence of different $\text{Fe}_3\text{O}_4@\text{C}$ NP concentrations.

Results and discussion

Characteristics of the $\text{Fe}_3\text{O}_4@\text{C}$ NPs

The approach described here is to embed Fe_3O_4 NPs onto the activated carbon (AC) surface. The SEM image was used in order to investigate the morphology of the synthesized $\text{Fe}_3\text{O}_4@\text{C}$ NPs. As can be seen in Figure 1, the SEM images show that $\text{Fe}_3\text{O}_4@\text{C}$ NPs are composed of spherical shaped particles and core-shell particles on the AC surface. The magnetite particle size appeared to depend on the duration over which the ammonia solution was added to the ferric and ferrous salt mixture; a shorter duration (about 5 min) produced smaller particles that “spiked” readily when placed near a magnet. Small magnetite particles are desirable, since they have large surface-to-volume ratios, large reactive surfaces, and strong magnetism.²⁸ The procedure for the synthesized $\text{Fe}_3\text{O}_4@\text{C}$ NPs involved coating or mixing the porous AC surface with a magnetic solution. This allowed the small magnetic particles, when formed, to be intimately mixed on the AC surface leading to a desirable structure for the $\text{Fe}_3\text{O}_4@\text{C}$ NPs (Figure 1).

The morphology, structure, and size of the $\text{Fe}_3\text{O}_4@\text{C}$ NPs were determined by TEM on different scale bars of 40–200 nm (Figure 2(a)–(c)). Figure 2(d) shows the histogram of particle size versus number of particles observed by TEM grid on the scale bar of 100 nm. The particle size distribution is in the range of 4–50 nm. It is clear from the histogram that the mean particle size of $\text{Fe}_3\text{O}_4@\text{C}$ NPs is 14.66 nm. The particles exhibited core-shell and spherical morphology. In general, magnetite NPs synthesized through co-precipitation tends to aggregate together. As can be seen from Figure 2, a random distribution of $\text{Fe}_3\text{O}_4@\text{C}$ NPs accrued, and due to the presence of Fe_3O_4 NPs, magnetization behavior was expected.

The EDS results shown in Figure 3 qualitatively determined the surface composition of the $\text{Fe}_3\text{O}_4@\text{C}$ NPs. The EDS spectra showed the strong peaks of Fe, O, and C. This confirms the existence of oxygen and iron in the sample. Therefore, it is assumed that Fe_3O_4 NPs are coated onto the surface of AC.

The UV-Vis absorption spectra of the $\text{Fe}_3\text{O}_4@\text{C}$ NPs (Figure 4) shows an absorption band in the region of 300–400 nm ($\lambda_{\text{max}}=300.46$ nm) which originates primarily from the absorption and scattering of UV radiation by magnetic NPs, and is in accordance with the previously reported literature.^{29,30}

As can be seen in Figure 5, the strong, broad peaks in the FTIR spectrum of the $\text{Fe}_3\text{O}_4@\text{C}$ NPs at about 560–570 cm^{-1} are due to the stretching vibrations of Fe–O. The peaks around 3300–3500 cm^{-1} and 1300–1650 cm^{-1} have been assigned to the stretching and bending vibrations of the H–O–H bond, respectively, showing the physical absorption of H_2O molecules on the surfaces. The spectrum also shows that the H–O–H bending vibration at about 1000–1600 cm^{-1} , typical of the H_2O molecule, is less intense. In addition, the second absorption band, between 900 and 1000 cm^{-1} , corresponds to the bending vibration associated with the O–H bond. The O–H in plane and out of plane bonds appear at 1583–1481 cm^{-1} and 935–838 cm^{-1} , respectively.³¹ These first two bands correspond to the hydroxy groups attached by the hydrogen bonds on the iron oxide surface, as well as the water molecules chemically adsorbed to the magnetic particle surfaces.³²

In addition, the absorption bands at 574 cm^{-1} correspond to the vibration of tetrahedral, which are indicative of formation of a spinel ferrite structure. The shouldering of the band corresponding to the tetrahedral site is observed for the sample. It is attributed to the Jahn–Teller effect (a geometric distortion of a non-linear molecular system) produced by the Fe^{2+} ions that causes local deformations in the lattice owing to the non-cubic component of the crystal field potential, and hence leads to the splitting of this band, corresponding to the tetrahedral site.³³ Finally, the band observed at 574 corresponds to Fe_3O_4 . However, after $\text{Fe}_3\text{O}_4@\text{C}$ NPs formation, there are shifts of notable peaks such as the O–H, C=C, and C–O stretches, indicating that reduction had occurred. This indicates that Fe_3O_4 NPs synthesized on the AC as a stabilizer.

The XRD analysis of $\text{Fe}_3\text{O}_4@\text{C}$ NPs is shown in Figure 6. The peaks located at diffraction angles of $2\theta=30.43^\circ$, 35.71° , 43.53° , 53.73° , 57.31° , and 62.99° represent the crystalline planes (220), (311), (400), (422), (511), and (440), respectively, which obviously show the crystalline cubic structure of the magnetite phase (Fe_3O_4) (no. 98-024-0798).^{34,35} The strongest reflection comes from the (311) plane, which denotes the spinel phase. Also, the spectrum obtained from the XRD profile shows typical peaks at $2\theta=26.6^\circ$, 44.68° which are related to AC in the (002) and (100) directions, respectively.³⁶ The results confirm that Fe_3O_4 NPs are successfully impregnated onto the AC surface.

The crystallite size of the nanocrystalline samples was measured from the X-ray line broadening analyses using the Debye–Scherrer formula after accounting for instrumental broadening (equation (1))^{37,38}

$$D_{\text{XRD}} = \frac{0.9\lambda}{\beta \cos \theta} \quad (1)$$

where λ is the wavelength of the X-ray used in Å, β is the line broadening at half the maximum intensity (full width at half maximum (FWHM) in radians in the 2θ scale), θ is the Bragg angle, D_{XRD} is the crystallite size in nm. The average of the particle size of $\text{Fe}_3\text{O}_4@\text{C}$ NPs was found to be 14.9 nm using Debye–Scherrer equation. The lattice parameter (a) and interplanar spacing (d_{hkl}) are determined by Bragg’s law.¹⁴ The values obtained are shown in Table 1. The lattice parameter (a) and interplanar spacing (d_{hkl}) for

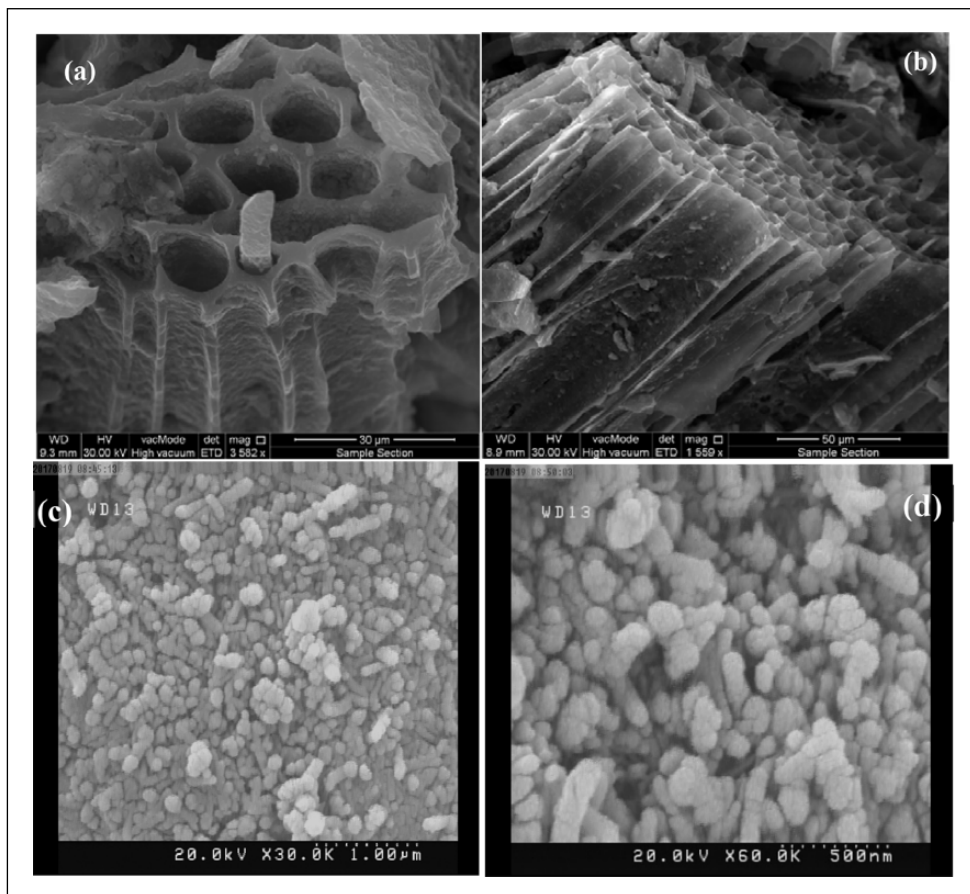


Figure 1. FESEM images of $\text{Fe}_3\text{O}_4@\text{C}$ NPs at different resolutions: (a) $30\ \mu\text{m}$, (b) $50\ \mu\text{m}$, (c) $1\ \mu\text{m}$, and (d) $500\ \text{nm}$.

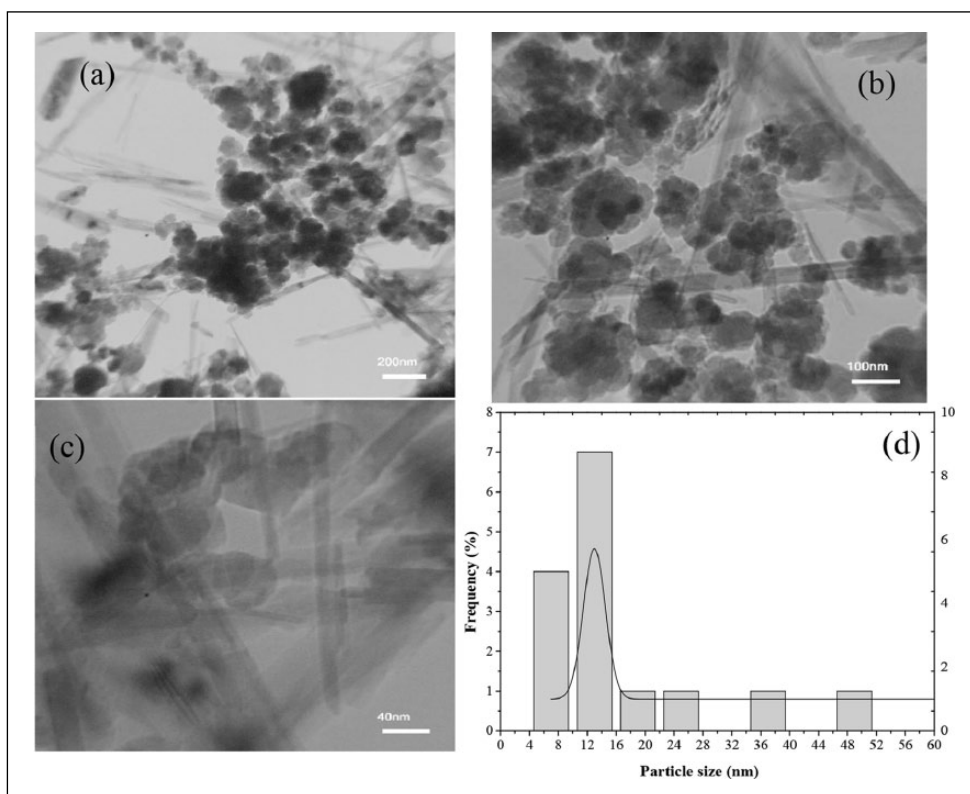


Figure 2. (a)–(c) TEM images of the size and morphology of $\text{Fe}_3\text{O}_4@\text{C}$ NPs with different resolutions of 40–200 nm. (d) Frequency distribution histogram for particle size of $\text{Fe}_3\text{O}_4@\text{C}$ NPs at 100-nm scale. It is clear from the histogram that the particle size distribution is in the range of 4–50 nm and the mean particle size of the $\text{Fe}_3\text{O}_4@\text{C}$ NPs is 14.66 nm.

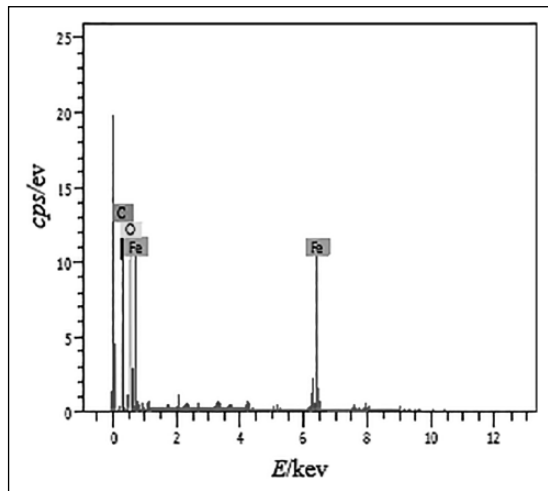


Figure 3. EDS results of Fe₃O₄@C NPs.

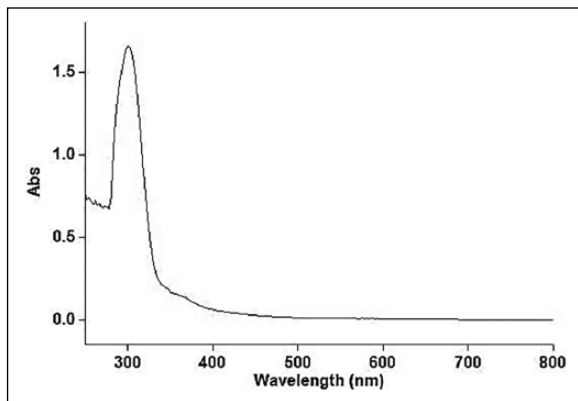


Figure 4. UV-Vis absorption spectrum for a diluted suspension of Fe₃O₄@C NPs.

the Fe₃O₄@C NPs are lower than the values reported for bulk magnetite JCPDS Card No. (79-0417) ($a=8.394$ and $d_{311}=2.531$), but these values are close to some of the values reported for Fe₃O₄ NPs in the literature.^{39,40}

Dislocation density (δ) is calculated with the crystalline size (D)⁴¹

$$\delta = \frac{1}{D^2} \quad (2)$$

Microstrain (ε) arises due to the lattice misfit, which varies on the deposition conditions and thus it is calculated by the formula (Table 1)⁴¹

$$\varepsilon = \frac{\beta \cos \theta}{4} \quad (3)$$

As can be seen in Table 1, the dislocation density (δ) for Fe₃O₄@C NPs (on diffraction angles at 30.43°–62.99° representing the crystalline planes) decreases with an increase in the crystallite size (D). Similarly, the microstrain (ε) increases with a decrease in the crystallite size.

Bactericidal activity of Fe₃O₄@C NPs

The antibacterial activities of the Fe₃O₄@C NPs were evaluated against three pathogenic bacteria (Gram-positive and

Gram-negative) at a concentration range of 11.50–36.30 mg mL⁻¹ in distilled water (Table 2 and Figure 7). The results of the antibacterial activities of the Fe₃O₄@C NPs at different concentrations (11.50, 20.10, 23.00, and 36.30 mg mL⁻¹) showed moderate antimicrobial activity against all the pathogenic strains with zones of inhibition ranging from 3.8 to 5.0 cm (Table 2). The zone of the clearance around each well after the incubation period confirms the antimicrobial activity of the synthesized Fe₃O₄@C NPs.

The results also revealed that the microorganisms are sensitive to the test samples at varying concentrations. The antibacterial activities of various concentrations of Fe₃O₄@C NPs on three bacterial strains are shown in Figure 8. The Fe₃O₄@C NPs showed antibacterial properties against both Gram-positive and Gram-negative bacterial strains. As the diameter of the zone of inhibition is high, we can conclude that the Fe₃O₄@C NPs are very effective antibacterial agents. From Table 2 and Figure 8, it is shown that on increasing the concentration of the NPs the antibacterial activity increases. In addition, a comparison of the literature data on the antibacterial activity of Fe₃O₄ NPs at different concentration ranges along with the results of this study is shown in Table 2. As can be seen, the antibacterial effects of Fe₃O₄ NPs on *Proteus mirabilis* have not been reported previously, and for *Pseudomonas aureginosa*, there is no effect on the zone of inhibition at high concentrations of Fe₃O₄ NPs. Whereas, in this work, Fe₃O₄@C NPs present antibacterial activities at different concentration ranges on three bacterial strains.

Conclusion

In this study, Fe₃O₄@C NPs were synthesized by a facile and rapid co-precipitation method. The prepared Fe₃O₄@C NPs were characterized by various techniques. The existence of strong signals with the highest percentage of Fe, O, and C in the EDS spectrum together with XRD, TEM, and field emission scanning electron microscope (FESEM) images confirmed the formation of crystalline Fe₃O₄@C NPs with a crystallite size of about 14 nm. For the synthesized NPs, XRD results demonstrated that the dislocation density and microstrain had decreased with an increase in the crystallite size. In addition, this study highlights the potential application of Fe₃O₄@C NPs as antibacterial agents against both Gram-positive and Gram-negative bacteria. These NPs can be explored for their topical application in pharmaceutical and biomedical industries.

Experiment

Materials

All chemical reagents used as starting materials were of analytical grade and were used without any further purification. Ferric chloride hexahydrate (FeCl₃·6H₂O, 98%), ferrous(II) sulfate heptahydrate (FeSO₄·7H₂O), AC powder, aqueous ammonia (NH₄OH; 35%), hydrochloric acid (HCl), and ethanol (C₂H₅OH) were purchased from SD Fine Chemicals Pvt. Ltd, India. We have used three bacterial species, Gram-positive (*Staphylococcus aureus* (*S. aureus*, ATCC25923)) and Gram-negative (*Proteus*

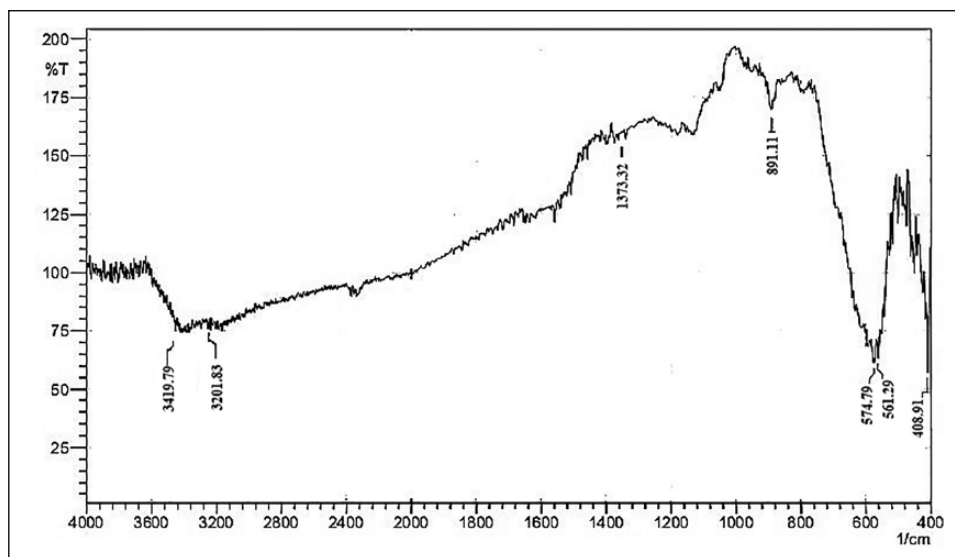


Figure 5. FTIR spectrum of $\text{Fe}_3\text{O}_4@\text{C}$ NPs.

Table 1. The values of observed “d,” crystallite size, dislocation density, strain, and h, k, l of $\text{Fe}_3\text{O}_4@\text{C}$ NPs.

Observed 2θ ($^\circ$)	Observed d (\AA) $a=8.3324\text{\AA}$	Crystallite size	Dislocation density (ρ) ($\times 10^{15}$ lines/ m^2)	Strain (ϵ) ($\times 10^{-3}$ lines/ m^4)	h	k	l
30.43	2.9367	23.8924	1.75	0.6145	2	2	0
35.71	2.5143	17.1873	3.38	0.7314	3	1	1
43.53	2.0787	17.6160	3.22	0.5900	4	0	0
53.73	1.7044	10.1944	9.62	0.8359	4	2	2
57.31	1.6061	10.3694	9.30	0.7744	5	1	1
62.99	1.4743	10.6842	8.76	0.6899	4	4	0

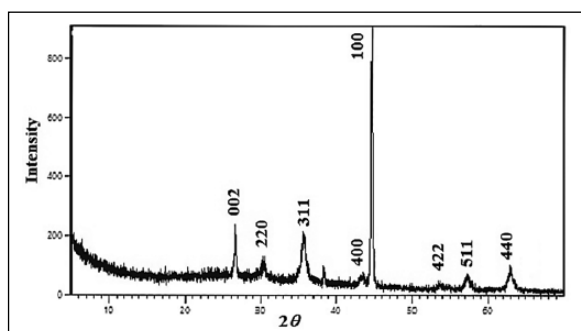


Figure 6. XRD of $\text{Fe}_3\text{O}_4@\text{C}$ NPs powder.

mirabilis (*P. mirabilis*, ATCC8759)) and (*Pseudomonas aureginosa* (*P. aureginosa*, ATCC27853)) obtained from the Department of Biology, Soran University in Kurdistan Regional Government (KRG), Iraq.

Synthesis of $\text{Fe}_3\text{O}_4@\text{C}$ NPs

$\text{Fe}_3\text{O}_4@\text{C}$ NPs were synthesized by the co-precipitation method as reported in other articles.^{45,46} AC was first dispersed in nitric acid (4.0M $\text{HNO}_3(\text{aq})$) at 130°C for 30 min under stirring to remove the impurities and then washed with distilled water until the filtrate was neutral. The Fe_3O_4 NPs were prepared by mixing a freshly prepared ferric-ferrous solution consisting of 4.0 mL of FeCl_3 (1.0M FeCl_3 in 2.0M

HCl), 1.0 mL of FeSO_4 (2.0M FeSO_4 in 2.0M HCl), and 0.10 g of AC powder with stirring for 3 min at the room temperature. The well-stirred mixture, 25 mL of 1.4M ammonia aqueous solution was added dropwise over a period of 10 min. During NH_3 addition, the suspension became dark brown at pH 6 and then black at pH 11. The precipitate was collected using a magnet and was washed with water several times to remove excess ammonia solution and was finally collected as a powder after being oven-dried at 50°C . Evidence suggests that the formation involves reduction of the Fe(III) salt into a Fe(II) intermediate on the AC surface as stabilizer⁴⁷



Screening of antibacterial activities

The well-diffusion technique⁴⁷ was used for investigating antibacterial effects of $\text{Fe}_3\text{O}_4@\text{C}$ NPs. About 300 μL of microbe cultures of age 18–24 h were added to Petri plates and nutrient agar was added. Once the medium has solidified, holes were made and each hole was packed with 100 μL (50 mg mL^{-1}) of $\text{Fe}_3\text{O}_4@\text{C}$ NPs powder in distilled water (different concentrations: 11.50–36.30 mg mL^{-1} in distilled water). The plates were wrapped in parafilm tape and transferred to an incubator and maintained at 37°C for 24 h. Negative and positive controls were used. The inhibition zones were recorded in centimeters.

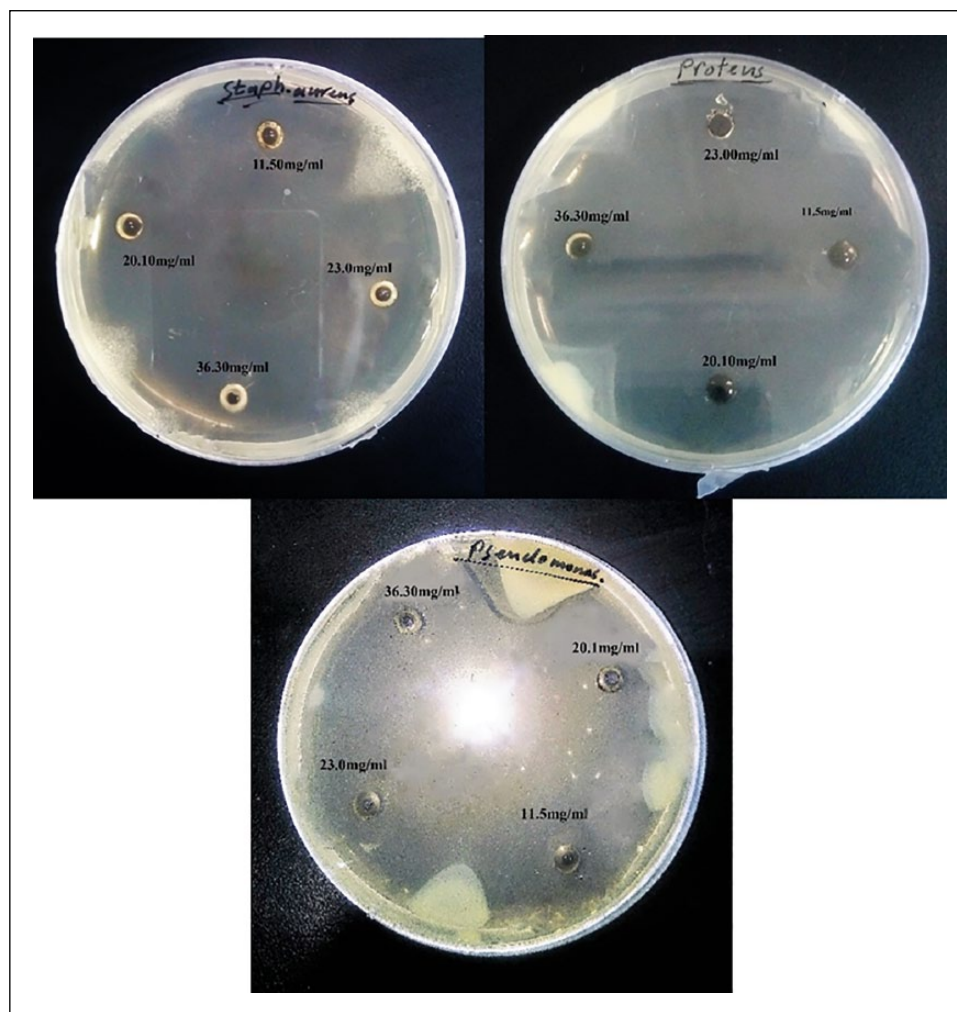


Figure 7. Study of antibacterial activity (zone of inhibition) of Fe₃O₄@C NPs on different microorganisms (*Staphylococcus aureus*, *Proteus mirabilis*, and *Pseudomonas aureginosa*).

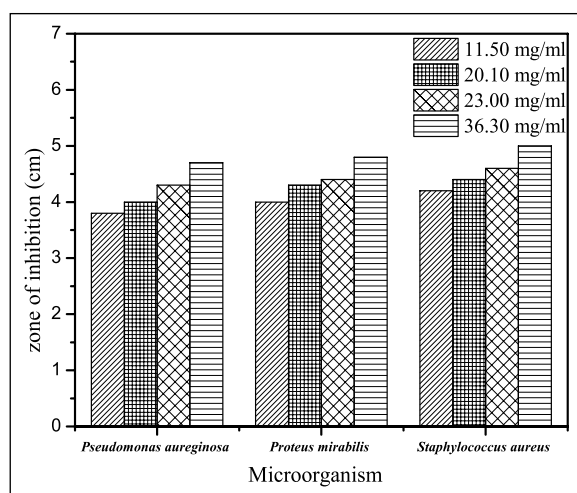


Figure 8. Effect of the antibacterial activities of the Fe₃O₄@C NPs at different concentrations on the zones of inhibition of microorganisms.

Measurement techniques

The synthesized Fe₃O₄@C NPs were characterized by SEM, TEM, EDS, XRD, FTIR, and UV-Vis spectroscopy.

The cross section morphology of the Fe₃O₄@C NPs was studied by high-resolution SEM (Quanta 450) equipped with EDS (Quantax EDS features the XFlash[®] 6 detector) at an accelerating voltage of 20 kV. A thin layer of gold was coated on the sample before microscopic analysis. Bright-field TEM images were recorded on a Philips EM 120 TEM at an accelerating voltage of 80 kV. The sample for TEM analysis was cut into slices of a nominal thickness of 100 nm using an ultra-microtome with a diamond knife on a Reichert Ultracut ultra-microtome at ambient temperature. The cut samples were supported on a copper mesh for this analysis. The XRD patterns of the sample were recorded at room temperature on a Philips powder diffractometer type (PW1373 goniometer) using Cu K α ($\lambda = 1.54060 \text{ \AA}$) radiation with a scanning rate of 2° min^{-1} in the 2θ range from 0° to 80° . Scanning was applied to for the selected diffraction peaks which were carried out in step mode (step size 0.01° , measurement time 0.5 s, accelerating voltage of 45 kV, an emission current of 40 mA) measurement. The absorbance spectrum of the Fe₃O₄@C NPs suspension after diluting a small aliquot was recorded using UV-Vis spectroscopy (Cary 100, tungsten halogen light sources). The presented results were obtained at room temperature. In addition, Fe₃O₄@C NPs were investigated by FTIR spectroscopy

Table 2. Comparison of the literature data on the antibacterial activity Fe₃O₄ NPs at different concentration ranges with the data of Fe₃O₄@C NPs used in this study.

Strain	Concentration of IONPs (mg mL ⁻¹)	Zone of inhibition (cm)
<i>Staphylococcus aureus</i>	This study	4.2, 4.4, 4.6, 5.0
	1 1.50, 20.10, 23.00, 36.30	
	Literature	1.2 ± 0.35 ⁴²
	50 ⁴² (10, 20, 30, 40, 50) ⁴³ (0.03, 0.3, 3) ⁴⁴ (25, 30, 40, 50, 60, 80, 100) ¹⁷	(5.0, 1.2, 1.8, 2.2, 3.0) ⁴³ — 1.0–1.5 ¹⁷
<i>Pseudomonas aureginosa</i>	This study	3.8, 4.0, 4.3, 4.7
	1 1.50, 20.10, 23.00, 36.30	
	Literature	0.0 ± 0.00 ⁴²
<i>Proteus mirabilis</i>	This study	4.2, 4.3, 4.4, 4.8
	1 1.50, 20.10, 23.00, 36.30	
	There are no reported data with IONPs.	—

IONPs: iron oxide nanoparticles.

(IRAffinity-1 Shimadzu Corp. A213750). Dried and powdered NPs were pelleted with potassium bromide (KBr). The spectra were recorded in the wavenumber range of 400–4000 cm⁻¹ and analyzed by subtracting the spectrum of pure KBr.

Acknowledgements

The authors thank Miss Somayeh Khezrian (PhD student) at Tehran University, Mr Shorish Mustafa Abdullah, Karzan Mohammed Khalid (Assistant Lecturer) at Soran University, Mr Karzan Abdulkareem Omar (Assistant Lecturer) at Koya University and Mr Pshtiwan Yusif (Assistant Lecturer) at Salahaddin University for recording the FESEM, FTIR, and UV-Vis spectra, respectively.


Declaration of conflicting interests

The author(s) declared no potential conflicts of interest with respect to the research, authorship, and/or publication of this article.

Funding

The author(s) received no financial support for the research, authorship, and/or publication of this article.

ORCID iD

S Mohammad Sajadi  <https://orcid.org/0000-0001-8284-5178>

References

- Nicoara G, Fratiloiu D, Nogues M, et al. *Mater Sci Forum* 1997; 235: 145–150.
- Prodan D, Chan C and Tronc E. *J Magn Magn Mater* 1999; 203: 63–65.
- Eglesias S, Leon Isidro LM and Lopez-Quintela MA. *J Non-Cryst Solids* 2007; 353: 829–831.
- Figuerola A, Corato RD, Manna L, et al. *Pharmacol Res* 2010; 62: 126–143.
- Predoi D, Kuncser V and Filoti G. *Rom Rep Phys* 2004; 56: 373–378.
- Iconaru SL, Prodan AM, Coustumer PL, et al. *J Chem* 2013; 2013: 1–6.
- Muhammad SU, Mohamed EE, Kamyar SS, et al. *Int J Nanomed* 2013; 4467: 145–150.
- Koo B, Xiong H and Slater MD. *Nano Lett* 2012; 12: 2429–2435.
- Du X, Wang C, Chen M, et al. *J Phys Chem* 2009; 113: 2643–2646.
- Lin S, Shen C, Lu D, et al. *J Carbon* 2013; 53: 112–119.
- Fukushima T, Sekizaqa K, Jin Y, et al. *Am J Physiol* 1993; 265: 67–72.
- Chemla YR, Crossman HL, Poon Y, et al. *P Natl Acad Sci USA* 2000; 97: 14268–14272.
- Ugelstad J, Berge A and Ellingsen T. *Prog Polym Sci* 1992; 17: 87–161.
- Liu Y, Gao Y and Xu C. *Chin Phys B* 2013; 22: 097503.
- Mohapatra M and Anand S. *Int J Eng Tech* 2010; 2: 127–146.
- Runowski M, Grzyb T and Lis S. *J Nanopart Res* 2012; 14: 1188–1197.
- Prabhu YT, Venkateswara Rao K, Siva Kumari B, et al. *Int Nano Lett* 2015; 5: 85–92.
- Corot C, Robert P, Idee JM, et al. *Adv Drug Deliv Rev* 2006; 58: 1471–1504.
- Zhao DL, Zeng XW, Xia QS, et al. *J Alloy Comp* 2009; 496: 215–218.
- Lu J, Ma S and Sun J. *Biomaterials* 2009; 30: 2919–2928.
- Bahadur D and Giri J. *J Biomed Mater Res B* 2003; 28: 639–656.
- Alexiou C, Arnold W, Klein RJ, et al. *Cancer Res* 2000; 60: 6641–6648.
- Jiang QL, Zheng SW and Hong RY. *Appl Surf Sci* 2014; 307: 224–233.
- Cheng FY, Su CH, Yang YS, et al. *Biomaterials* 2005; 26: 729–738.
- Pareta RA, Taylor E and Webster TJ. *Nanotechnology* 2008; 19: 265101–265107.
- Lee C, Kim JY, Lee WI, et al. *Environ Sci Technol* 2008; 42: 4927–4933.
- Taylor EN and Webster TJ. *Int J Nanomed* 2009; 4: 145–152.
- Madrakian T, Afkhami A, Mahmood-Kashani H, et al. *J Iran Chem Soc* 2013; 10: 481–489.
- Koutzarova T, Kolev S, Ghelev C, et al. *Phys Stat Sol* 2006; 3: 1302–1308.
- Obaid R, Subash C and Sharif A. *Mater Chem Phys* 2012; 132: 196–202.

31. Ling Z, Rong H and Hong-Chen G. *Appl Surf Sci* 2006; 253: 2611–2617.
32. Lopez JA, González F, Bonilla FA, et al. *Rev Latinam Metal Mat* 2010; 30: 60–66.
33. Ahn Y, Choi EJ and Kim EH. *Rev Adv Mater Sc* 2003; 5: 477–502.
34. Wang X, Zhao Z, Qu J, et al. *J Phys Chem Solids* 2010; 71: 673–676.
35. Yan H, Zhang J, You C, et al. *Mater Chem Phys* 2009; 113: 46–52.
36. Taleshi F and Hosseini AA. *J Nanostruct Chem* 2012; 3: 1–5.
37. Cullity BD. *Elements of X-ray diffraction*. 2nd ed. Philippines: Addison-Wesley, 1978.
38. Pal J and Chauhan P. *Mater Charact* 2009; 60: 1512–1516.
39. Victoria LC-D and Carlos R. *J Magn Magn Mater* 2007; 314: 60–67.
40. Zhang Y, Yang Z, Yin D, et al. *J Magn Magn Mater* 2010; 322: 3470–3475.
41. Gubicza J, Szepvolgyi J, Mohai I, et al. *Mat Sci Eng A* 2000; 280: 263–269.
42. Sudhanshu SB, Jayanta KP and Krishna PNP. *World J Nano Sci Eng* 2012; 2: 196–200.
43. Manyasree D, Kiranmayi P and Ravi Kumar RV. *Indo Am J Pharm Res* 2016; 6: 2231–6876.
44. Tran N, Mir M, Mallik D, et al. *Int J Nanomed* 2010; 5: 277–283.
45. Predoi D. *J Nanomater Biostruct* 2007; 2: 169–173.
46. Sophie L, Delphine F and Marc P. *Chem Rev* 2008; 108: 2064–2110.
47. Behera SSH Patra JK and Thatoi H. *World J Nano Sci Eng* 2012; 2: 196–200.